EFFECTIVE EXHAUST GAS TREATMENT CATALYST WITH RESISTANCE TO SULFUR DIOXIDE

by

Yang Cheng

A thesis submitted to The Johns Hopkins University in conformity with

the requirements for the degree of Master of Science

Baltimore, Maryland

May 2020

Abstract

Air pollution threatens human health and quality of life. Carbon monoxide (CO), one of the primary ambient air contaminants, is mainly introduced by motor vehicle emissions. To protect human health and comply with emission regulations, catalytic converter has been installed on vehicles. However, low efficiency in cold-start and warm-up period and catalyst poisoning are still key problems for catalytic converter. In this work, treating sulfur dioxide (SO_2) as poisoning source, we present how to seek catalyst candidates for conversion process of CO which are stable against SO_2. Inspired by the oxygen vacancy tolerance of CeO_2 and ABO_3 perovskite compounds, all existing binary oxides and ABO_3 perovskite compounds were chose as subjects. We constructed phase diagram and analyze stability through interfacial reactions by using Pymatgen. Because the catalytic mechanism could be expressed by oxygen vacancy formation energy, DFT calculations were applied on stable oxides to get oxygen vacancy formation energies on bulk and surface. If one oxide is stable against SO_2 and has appropriate oxygen vacancy formation energy, it could be a promising catalyst candidate for exhaust gas treatment. Most importantly, it is an auspicious approach to analyze stability in specific environment (temperature and partial pressure) by constructing phase diagram and considering interfacial reactions through Pymatge.

Primary Reader and Advisor: Tim Mueller

Acknowledgments

This work was supported by BASF Corporation. I acknowledge computational resources provided by the Maryland Advanced Research Computing Center (MARCC). I would like to express my sincere gratitude to Prof. Tim Mueller and everyone in our lab, Chenyang Li, Alberto Hernandez, Liang Cao, Yunzhe Wang, Chuhong Wang, Sukriti Manna and Shanping Liu. I would like to thank my parents, my friends and Senior Academic Program Coordinator Jeanine Majewski who have supported and helped me all the way.

Contents

List of Tables

List of Figures

Chapter 1

Introduction

Air pollution occurs when substances capable of change natural characteristics of the air are introduced into earth's atmosphere. Common sources of air pollution include household fuel and device, vehicles, industrial facilities (factories), and forest fire. Air pollution is associated with a broad spectrum of acute and chronic illness. [1-3] Globally, it is estimated to cause about 29% of lung cancer deaths, 43% of chronic obstructive pulmonary disease (COPD) deaths, about 25% of ischaemic heart disease deaths and 24% of stroke deaths. [4] The 2005 *WHO Air quality guidelines* offer global guidance on thresholds and limits for key air pollutants that pose health risks, on the basis of expert evaluation of current scientific evidence for particulate matter (PM), ozone (O_3), nitrogen dioxide (NO_2) and sulfur dioxide (SO_2). [5] In Climate and Clean Air Coalition, member countries and organizations concentrate on reducing the so-called short-lived climate pollutants (SLCPs): black carbon, methane, ozone and hydrofluoro carbons. Reduction of these could bring significant results in both slowing global warming and improving health in the short term. [6] Moreover, carbon monoxide (CO) is also one of the most important ambient air contaminants. It is well known that carbon monoxide competes with oxygen at the heme binding site and modifies conformation of hemoglobin. The reduced oxygen capacity can have negative impacts on organs with symptoms like impaired concentration, slow reflexes, confusion, unconsciousness and even death. [7]

Although very high level of CO is not likely to be achieved outdoors, short-term exposure to high concentration of CO for people with heart diseases is dangerous. In addition, recent experimental evidences suggest CO would impair neurodevelopment and cause behavioral disorders in children. [8] Motor vehicle emissions are the primary source of ambient CO. According to NEI, motor vehicle emissions contribute nearly 60% of the total CO emitted nationally in 2008. To protect health and environment, Federal programs provide for nationwide reductions in emissions of air pollutants through the Federal motor vehicle and motor vehicle fuel control program, which involves controls for emissions from moving sources and controls for the fuels used by these sources and new source performance standards for stationary sources. [9, 10] In addition, the United States Environmental Protection Agency has *set National Ambient Air Quality Standards for Carbon Monoxide* to state maximum amounts of carbon monoxide to be present outdoors.

The U.S. Environmental Protection Agency set emission standards for hydrocarbons (HC), carbon monoxide (CO) and nitrogen oxide (NO_x) for vehicles starting with the 1975 model year. The stricter regulation ignited the development and implementation of a range of technologies, including catalytic converters. Most gasoline-powered vehicles beginning with 1975 model vehicles must be equipped with catalytic converters to reduce emissions. [11-13] A catalytic converter is an exhaust emission control device that reduces toxic gases and pollutants in exhaust gas from an internal combustion engine into less-toxic pollutants by catalyzing a redox reaction (an oxidation and a reduction reaction). [14] There are typically two types of catalytic converters, “two-way” and “three-way” converters. The two-way catalytic converters are widely used in diesel engine, converting carbon monoxide to carbon dioxide, and converting hydrocarbons to carbon dioxide and water simultaneously. The three-way catalytic converters have one

additional task reducing nitrogen oxides to nitrogen. The current catalyst used in converters generally contain the precious metals rhodium, platinum and palladium, ceria (CeO_2), γ-alumina (Al_2O_3), and other metal oxides. [15] Ceria (CeO_2) plays an important role in catalytic process, owing to its excellent redox properties and oxygen storage capacity. Carbon monoxide (CO) reacts with oxygen in ceria (CeO_2) directly, forming carbon dioxide (CO_2) and leaving oxygen vacancies in CeO_2. The oxygen vacancies are filled by gas-phase O_2 subsequently. The renewed CeO_2 provides CO oxidation with oxygen continually. The conversion efficiency of new catalytic converter could achieve 80% ~ 90%. [16] However, catalyst would be inactivated when it is during cold-start and warm-up period or when catalyst poisoning occurs. [14, 17] Catalyst poisoning refers to the partial or total deactivation of a catalyst when the catalytic converter is exposed to exhaust containing substances that coat the working surfaces and then cannot contact and react with the exhaust. [14, 18] Sulfur dioxide (SO_2) is one of the most important examples poisoning catalytic converters. [19]

In this work, we present how to find oxides capable of being catalyst for conversion process of CO, which will be resistant to SO_2 in the meanwhile. Oxygen vacancies are formed and eliminated in the oxides during the whole catalytic process, the same as catalytic process of ceria (CeO_2) described above. If oxides have suitable oxygen vacancy formation energy, they can catalyze the redox reaction from CO to CO_2. Phase diagram shows phases coexisting in equilibrium at given conditions (temperature, pressure, volume, etc.). Analyzing the interfacial reactions between specific oxide and SO_2 based on phase diagram, it is easy to decide whether the oxide is stable against SO_2.

Chapter 2

Materials and Methods

2.1 Materials

Inspired by high tolerance of oxygen vacancy for CeO_2 and ABO_3 perovskite compounds, [20, 21] our study is starting with oxides. To find oxides competent for exhaust CO treatment, all binary oxides and ABO_3 perovskite compounds are selected as subjects of this work. In order to get oxides list and corresponding structure, this study refers to three database and dataset, including the Inorganic Crystal Structure Database (ICSD), [22, 23] the Materials Project, [24] and the Open Quantum Materials Database (OQMD). [25, 26]

2.2 Density functional theory (DFT) calculations

All compounds were calculated by density functional theory using the Vienna Ab initio Simulation Package (VASP) [27] version 5.4 using "accurate" precision. Perdew–Burke–Ernzerhof (PBE) [28] projector augmented wave (PAW) [29] potentials were used for throughout. To take into account of possible spin polarization in the material, all calculations are set to be spin polarized. The convergence criteria for the electronic self-consistent iteration and ionic relaxation loop were set to 10^{-5} eV and 10^{-4} eV. The k-point grid was generated using the k-point grid server [30] with a minimum periodic distance of 30 Å. For system including d or f orbitals, especially for transition metal oxides, GGA+U formalism of Dudarev [31] is used. To keep consistent with stability analysis, we used effective U value of U – J (denoted as U_{eff}) from the Materials Project. U is the Hubbard parameter which reflects the strength of the on-site Coulomb interaction and J is the

parameter which adjusts the strength of the exchange interaction. U_{eff}-values used in calculations are shown in Table 1. The bulk models were built with around 10 Angstroms between translationally equivalent images. For surface models, 9-angstrom thick slabs with around 15 angstroms of vacuum were performed on different facet of binary oxides and ABO_3 perovskite compounds, respectively.

Table 1. U_{eff} values for transition metal used in DFT calculations

Transition Metal	U_{eff} (eV)
Co	3.32
Cr	3.7
Fe	5.3
Mn	3.9
Mo	4.38
Ni	6.2
V	3.25
W	6.2

2.3 Calculation of vacancy formation energy

A single oxygen vacancy formation energy is given by [26, 32, 33, 34]

$$E_v^O = \frac{1}{m}[E_{tot}(defect\ supercell) + m\mu_O - nE_{tot}(pristine\ cell)] \quad (1)$$

Where E_v^O is the oxygen vacancy formation energy, $E_{tot}(defect\ supercell)$ is the total

energy of the defective superlattice with oxygen vacancy, $E_{tot}(pristine\ cell)$ is the total energy of perfect pristine cell, and μ_O is the chemical potential of oxygen. Parameter m describes the number of oxygen atom removed from the supercell. For bulk models, m = 1. And for slab models, to keep symmetry of slab structure, m = 2. Parameter n here is assigned according to the relationship between extended supercell and pristine cell.

The oxygen chemical potential is related to temperature and oxygen partial pressure by the following equations [35]:

$$\mu_O = \frac{1}{2}\mu_{O_2}(T, P_{O_2}) = \frac{1}{2}\left(\mu_{O_2}(T, P_O) + kTln\frac{P_{O_2}}{P_O}\right) \quad (2)$$

$$\approx \frac{1}{2}H_{O_2}(T, P_O) - \frac{1}{2}TS_{O_2}(T, P_O) + \frac{1}{2}kTln\frac{P_{O_2}}{P_O} \quad (3)$$

Where P_{O_2} is the partial pressure of oxygen, p_O is the reference oxygen partial pressure, which for this study is 101325 Pa, $S_{O_2}(T, P_O)$ is the per molecule entropy of oxygen at the reference partial pressure and temperature T, $\mu_{O_2}(T, P_O)$ is the oxygen chemical potential at the reference partial pressure and temperature T, $H_{O_2}(T, P_O)$ is the per molecule oxygen enthalpy at the reference partial pressure and temperature T, and k is Boltzmann's constant.

2.4 Stability analysis

Phase diagram shows the conditions (pressure, temperature, volume, etc.) at which distinct phases occur and coexist at equilibrium. [36, 37] Thermodynamic stability was assessed using an energy convex hull construction. The convex hull consists of phases that have an energy lower than any other phase or linear combination of phases at the respective compositions. [26] All structures, except ground state, have an energy that falls above the set of tie lines that connects the energy of the ground states. [38] In other words, unstable phases have energies higher than convex hull energy, like what is shown in Figure 1. Unstable spinel MnO_2 has higher formation energy than convex hull. This

energy above hull could be used to determine the phase stability. In theory, for a given phase, it is stable if convex hull distance (energy above hull) is zero. In this work, we slightly loosen this strict restriction to account for near-stable compounds and possible uncertainties/errors associated with DFT. Concretely, oxides with an energy above hull below 0.025 eV per atom are treated as stable phases. [26]

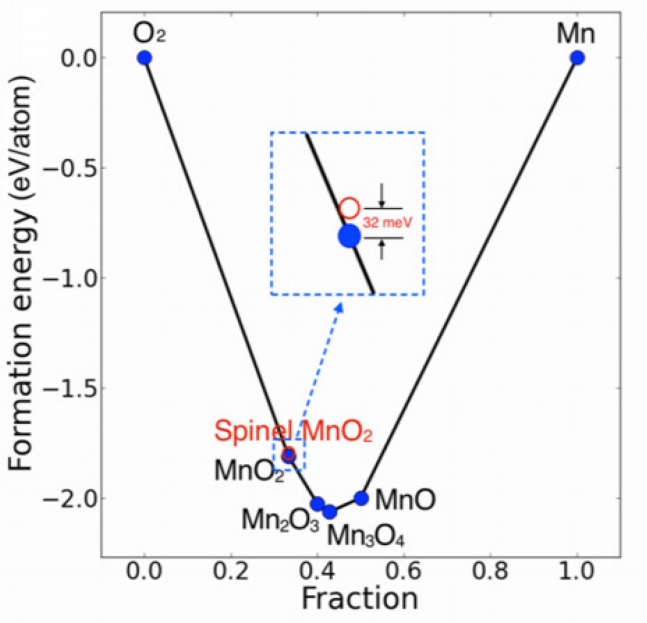

Figure 1. Phase diagram of Mn – O

Additionally, the stability of one phase against other phases, was analyzed by interfacial reactions. In phase diagram, the lines joining the compositions in equilibrium are known as tie-lines. [39] The tie lines are projections of convex hull construction into compositional space, representing compositions where two phases coexist. Ce-O-S ternary phase diagram is shown in Figure 2. In the figure, there is no line connecting stable phase of CeO_2 and SO_2. It means that both of these two compounds are stable at that condition (temperature and pressure), but they do not coexist but produce $Ce(SO_4)_2$. The stability analysis between two unconnected phases is impeded without the pre-

requisite of coexistence in equilibrium. To analyze it, interfacial reaction is applied. Interfacial reactions can occur when two contacting materials are not thermodynamically stable against each other. The reaction energy reflects the reactivity of the interface. [40] Hence, with interfacial reaction, it is apparent what would occur when mixing ratio changes along the tie line connecting oxides and specific gas. And comparing the interfacial reaction energy, we could analyze the stability of oxides against gas phases. Though it is difficult to investigate interfacial reactions experimentally because of the accessing challenges and limited thickness, [40] it is a great way to take advantage of "interface_reactions" module [41] in Pymatgen (Python Materials Genomics), which is a robust, open-source Python library for materials analysis. [42]

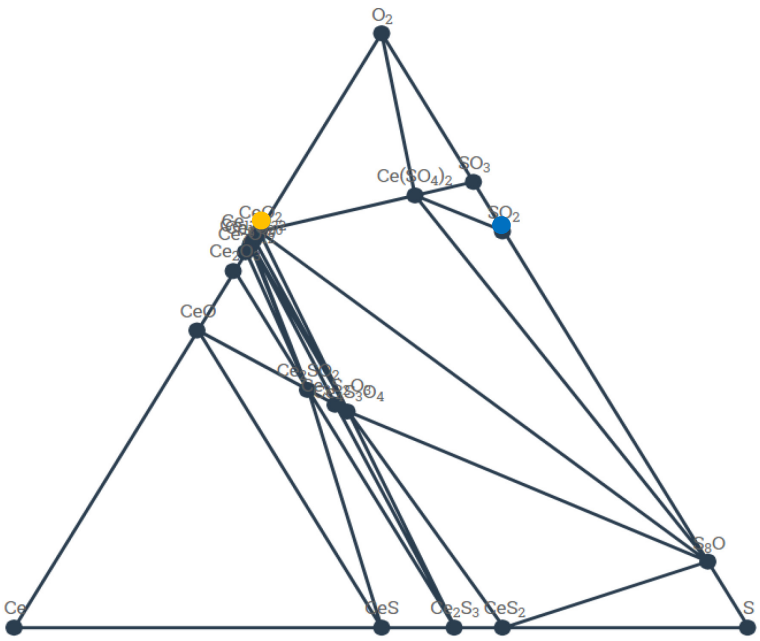

Figure 2. Ce-O-S ternary phase diagram

To analyze the stability of oxides against specific gas in different environment, we should consider the effect of temperature and partial pressure on energy, which is shown

as following equation:

$$\mu = H - T(S - kln\frac{P}{P_0}) \qquad (4)$$

Where μ is the chemical potential of gas used to construct phase diagram, H and S are enthalpy and entropy, respectively, P is partial pressure of specific gas, P_0 is reference pressure for gas, equal to 101325 Pa in this study, and k is Boltzmann's constant. In this work, we set 9 test temperatures, ranging from 298 K to 1098 K. And partial pressures used in this work are listed in Table 2.

Table 2. Partial pressure set for gas phases

Gas Phases	Concentrations (Total pressure = 1 atm)
SO_2	15 ppm
NO	150 ppm
O_2	10%
H_2O	5%
CO	1000 ppm

For enthalpy part, to keep consistent with the Pymatgen, energies from Materials Project were used as enthalpy values. For entropy part, entropy values at 298 K were used for oxides, and equation 5 was used to calculate entropy in different environment (temperatures and partial pressure) for gas phases.

$$S = Aln(t) + Bt + C\frac{t^2}{2} + D\frac{t^3}{3} - \frac{E}{2t^2} + G \qquad (5)$$

Where A, B, C, D, E and G are parameters from NIST, listed in Table 3 to Table 18. [43]

Table 3. Thermochemistry data for CH_4

Temperature (K)	298. - 1300.	1300. - 6000.
A	-0.70303	85.81217
B	108.4773	11.26467
C	-42.5216	-2.11415
D	5.862788	0.13819
E	0.678565	-26.4222
F	-76.8438	-153.533
G	158.7163	224.4143
H	-74.8731	-74.8731
Reference	Chase, 1998	Chase, 1998
Comment	Data last reviewed in March, 1961	Data last reviewed in March, 1961

Table 4. Thermochemistry data for CO

Temperature (K)	298. - 1300.	1300. - 6000.
A	25.56759	35.1507
B	6.09613	1.300095
C	4.054656	-0.20592
D	-2.6713	0.01355
E	0.131021	-3.28278
F	-118.009	-127.838
G	227.3665	231.712
H	-110.527	-110.527
Reference	Chase, 1998	Chase, 1998
Comment	Data last reviewed in September, 1965	Data last reviewed in September, 1965

Table 5. Thermochemistry data for CO_2

Temperature (K)	298. - 1200.	1200. - 6000.
A	24.99735	58.16639
B	55.18696	2.720074
C	-33.6914	-0.49229
D	7.948387	0.038844
E	-0.13664	-6.44729
F	-403.608	-425.919
G	228.2431	263.6125
H	-393.522	-393.522
Reference	Chase, 1998	Chase, 1998
Comment	Data last reviewed in September, 1965	Data last reviewed in September, 1965

Table 6. Thermochemistry data for H_2

Temperature (K)	298. - 1000.	1000. - 2500.	2500. - 6000.
A	33.06618	18.56308	43.41356
B	-11.3634	12.25736	-4.29308
C	11.43282	-2.85979	1.272428
D	-2.77287	0.268238	-0.09688
E	-0.15856	1.97799	-20.5339
F	-9.9808	-1.14744	-38.5152
G	172.708	156.2881	162.0814
H	0	0	0
Reference	Chase, 1998	Chase, 1998	Chase, 1998
Comment	Data last reviewed in March, 1977; New parameter fit October 2001	Data last reviewed in March, 1977; New parameter fit October 2001	Data last reviewed in March, 1977; New parameter fit October 2001

Table 7. Thermochemistry data for H_2O

Temperature (K)	298. - 500. 500. - 1700.	1700. - 6000.
A	-203.6060 30.09200	41.96426
B	1523.290 6.832514	8.622053
C	-3196.413 6.793435	-1.49978
D	2474.455 -2.534480	0.098119
E	3.855326 0.082139	-11.1576
F	-507.429	-272.18
G	-488.7163 223.3967	219.7809
H	-527.657	-241.826
Reference	Chase, 1998	Chase, 1998
Comment	Data last reviewed in March, 1979	Data last reviewed in March, 1979

Table 8. Thermochemistry data for H_2O_2

Temperature (K)	298. - 1500.
A	34.25667
B	55.18445
C	-35.1544
D	9.08744
E	-0.42216
F	-149.91
G	257.0604
H	-136.106
Reference	Chase, 1998
Comment	Data last reviewed in December, 1960

Table 9. Thermochemistry data for H_2S

Temperature (K)	298. - 1400.	1400. - 6000.
A	26.88412	51.22136
B	18.67809	4.147486
C	3.434203	-0.64357
D	-3.3787	0.041621
E	0.135882	-10.4639
F	-28.9121	-55.8761
G	233.3747	243.69
H	-20.502	-20.502
Reference	Chase, 1998	Chase, 1998
Comment	Data last reviewed in June, 1977	Data last reviewed in June, 1977

Table 10. Thermochemistry data for H_2SO_4

Temperature (K)	298. - 1200.	1200. - 6000.
A	47.28924	139.2289
B	190.3314	9.513663
C	-148.13	-1.79558
D	43.86631	0.118069
E	-0.74002	-15.6149
F	-758.953	-813.098
G	301.2961	416.1854
H	-735.129	-735.129
Reference	Chase, 1998	Chase, 1998
Comment	Data last reviewed in September, 1977	Data last reviewed in September, 1977

Table 11. Thermochemistry data for N_2

Temperature (K)	100. - 500.	500. - 2000.	2000. - 6000.
A	28.98641	19.50583	35.51872
B	1.853978	19.88705	1.128728
C	-9.64746	-8.59854	-0.1961
D	16.63537	1.369784	0.014662
E	0.000117	0.527601	-4.55376
F	-8.67191	-4.9352	-18.9709
G	226.4168	212.39	224.981
H	0	0	0
Reference	Chase, 1998	Chase, 1998	Chase, 1998
Comment	Data last reviewed in March, 1977; New parameter fit January 2009	Data last reviewed in March, 1977; New parameter fit January 2009	Data last reviewed in March, 1977; New parameter fit January 2009

Table 12. Thermochemistry data for N_2O

Temperature (K)	298. - 1400.	1400. - 6000.
A	27.67988	60.30274
B	51.14898	1.034566
C	-30.6445	-0.193
D	6.847911	0.01254
E	-0.15791	-6.86025
F	71.24934	48.6139
G	238.6164	272.5002
H	82.04824	82.04824
Reference	Chase, 1998	Chase, 1998
Comment	Data last reviewed in December, 1964	Data last reviewed in December, 1964

Table 13. Thermochemistry data for NO

Temperature (K)	298. - 1200.	1200. - 6000.
A	23.83491	35.99169
B	12.58878	0.95717
C	-1.13901	-0.14803
D	-1.49746	0.009974
E	0.214194	-3.00409
F	83.35783	73.10787
G	237.1219	246.1619
H	90.29114	90.29114
Reference	Chase, 1998	Chase, 1998
Comment	Data last reviewed in June, 1963	Data last reviewed in June, 1963

Table 14. Thermochemistry data for NO_2

Temperature (K)	298. - 1200.	1200. - 6000.
A	16.10857	56.82541
B	75.89525	0.738053
C	-54.3874	-0.14472
D	14.30777	0.009777
E	0.239423	-5.45991
F	26.17464	2.846456
G	240.5386	290.5056
H	33.09502	33.09502
Reference	Chase, 1998	Chase, 1998
Comment	Data last reviewed in September, 1964	Data last reviewed in September, 1964

Table 15 Thermochemistry data for NO_3

Temperature (K)	298. - 1100.	1100. - 6000.
A	11.22316	82.27418
B	166.3889	0.487106
C	-148.446	-0.09877
D	47.40598	0.006853
E	-0.17679	-6.26495
F	61.00858	29.22311
G	221.7679	326.2528
H	71.128	71.128
Reference	Chase, 1998	Chase, 1998
Comment	Data last reviewed in December, 1964	Data last reviewed in December, 1964

Table 16. Thermochemistry data for O_2

Temperature (K)	100. - 700.	700. - 2000.	2000. - 6000.
A	31.32234	30.03235	20.91111
B	-20.2353	8.772972	10.72071
C	57.86644	-3.98813	-2.0205
D	-36.5062	0.788313	0.146449
E	-0.00737	-0.7416	9.245722
F	-8.90347	-11.3247	5.337651
G	246.7945	236.1663	237.6185
H	0	0	0
Reference	Chase, 1998	Chase, 1998	Chase, 1998
Comment	Data last reviewed in March, 1977; New parameter fit January 2009	Data last reviewed in March, 1977; New parameter fit January 2009	Data last reviewed in March, 1977; New parameter fit January 2009

Table 17. Thermochemistry data for SO_2

Temperature (K)	298. - 1200.	1200. - 6000.
A	21.43049	57.48188
B	74.35094	1.009328
C	-57.7522	-0.07629
D	16.35534	0.005174
E	0.086731	-4.0454
F	-305.769	-324.414
G	254.8872	302.7798
H	-296.842	-296.842
Reference	Chase, 1998	Chase, 1998
Comment	Data last reviewed in June, 1961	Data last reviewed in June, 1961

Table 18. Thermochemistry data for SO_3

Temperature (K)	298. - 1200.	1200. - 6000.
A	24.02503	81.99008
B	119.4607	0.622236
C	-94.3869	-0.12244
D	26.96237	0.008294
E	-0.11752	-6.70369
F	-407.853	-437.659
G	253.5186	330.9264
H	-395.765	-395.765
Reference	Chase, 1998	Chase, 1998
Comment	Data last reviewed in September, 1965	Data last reviewed in September, 1965

Chapter 3

Results and Discussion

3.1 Materials list for analysis

According to ICSD, there are 3821 binary oxides and 176 ABO_3 perovskite oxide structures. According to high-throughput dataset from OQMD, there are 5329 ABO_3 perovskite compounds, created by substituting 73 metals and semi-metals of the periodic table of the elements. Considering energy above convex hull from Materials Project, there are 244 perfect binary oxides totally. Refer to stability value in ABO_3 dataset, there are 308 stable ABO_3 perovskite compounds. In this work, 0.025 eV/atom was used as the criteria for thermodynamic stability, because we planned to slightly loosen this restriction to account for nearly-stable compounds and possible uncertainties/errors associated with DFT. [26] In summary, there are 244 binary oxides and 308 ABO_3 perovskite compounds ready for following analysis. Figure 3 shows process how we set criteria and choose oxides as candidates in this work.

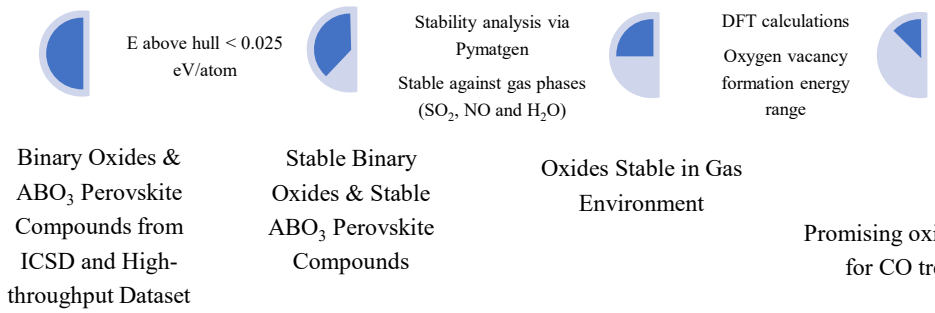

Figure 3 Flowchart for Analysis

3.2 Vacancy formation energy range

For oxides, the catalyst mechanism is described by the following reactions:

$$M_X O_{Y-\delta} + \frac{1}{2} O_2 \rightarrow M_X O_Y \quad (6)$$

$$M_X O_Y + CO \rightarrow M_X O_{Y-\delta} + CO_2 \quad (7)$$

$$CO + \frac{1}{2} O_2 \rightarrow CO_2 \quad (8)$$

Where $M_X O_Y$ is perfect oxide and $M_X O_{Y-\delta}$ is oxide with oxygen vacancy. Reaction 6 and 7 describe how oxides catalyze the CO redox reaction. Reaction 8 is exactly the CO redox reaction, the overall reaction for the catalyzing process.

To analyze whether the oxide catalyze the CO redox reaction successfully, we calculated Gibbs free energy for reaction 6 and 7. The following equations show how to get Gibbs free energy for reaction 6, 7 and 8:

$$\Delta G_1 = \Delta H_1 - T\Delta S_1 + \frac{1}{2} kT ln \frac{p_{O_2}}{p_O} \quad (9)$$

$$\Delta G_2 = \Delta H_2 - T\Delta S_2 + kT ln \frac{p_{CO_2}}{p_{CO}} \quad (10)$$

$$\Delta G_3 = \Delta H_3 - T\Delta S_3 + kT ln \frac{p_{CO_2}}{p_{O_2}^{\frac{1}{2}} p_{CO}} \quad (11)$$

WhereΔG is to change of reaction Gibbs free energy, ΔH and ΔS are change of reaction enthalpy and entropy, respectively, the subscripts of these three terms (1, 2 and 3) corresponds to for reaction 6, 7 and 8, respectively, the p_{O_2}, p_{CO}, and p_{CO_2} are partial pressure of O_2, CO and CO_2 respectively, p_O is the reference oxygen partial pressure, which for this study is 101325 Pa. Comparing equation 1 and 9, the relationship between them is,

$$\Delta G_1 = -E_v^O \quad (12)$$

Because of the relationship between reaction 6, 7 and 8, ΔG_2 could be expressed by using ΔG_1 and ΔG_3,

$$\Delta G_2 = \Delta G_3 - \Delta G_1 = \Delta G_3 + E_v^O \qquad (13)$$

To make sure the catalytic processes occur spontaneously, $\Delta G_1 < 0$ and $\Delta G_2 < 0$. A calculated range for oxygen vacancy formation energy was achieved as standard for catalyst,

$$0 < E_v^O < -\Delta H_3 + T[S(CO_2) - S(CO)] - kTln\frac{p_{CO_2}}{p_{O_2}^{\frac{1}{2}} p_{CO}} \qquad (14)$$

We should consider the gas phases energy correction before calculating the energy range, because the gas-phase thermodynamic reaction energies calculated with DFT are not consistent with experimental values. [44] According to the standard about oxygen vacancy formation energy obtained in equation 14, it is required to calculate energy of CO, O_2 and CO_2. We compared calculated and experimental gas-phase reaction enthalpies to determine whether it was necessary to apply energy correction for gas phases, applying the same methods as Cao et al. [44] used. And corrections for oxygen are 1.36 eV and 1.252 eV for transition metal oxides [45] and non-transition metal oxides, [46] respectively. We chose 8 reactions and compared the reaction energies from DFT and experimental reference data, and then used the average of these differences as systematic error. The reactions used are listed as reaction # 1 to # 8 in Table 19.

Table 19. Reactions used for gas-phase ΔH comparison (at 25 °C and 101325 Pa) [44]

Reaction #	Reactions containing	Reaction
1	CO_2 (g)	$4H_2 + CO_2 \rightarrow CH_4 + 2H_2O$
2		$\frac{7}{2}H_2 + CO_2 \rightarrow \frac{1}{2}C_2H_6 + 2H_2O$
3		$3H_2 + CO_2 \rightarrow \frac{1}{2}C_2H_4 + 2H_2O$
4		$\frac{5}{2}H_2 + CO_2 \rightarrow \frac{1}{2}C_2H_2 + 2H_2O$
5	CO (g)	$3H_2 + CO \rightarrow CH_4 + H_2O$
6		$\frac{5}{2}H_2 + CO \rightarrow \frac{1}{2}C_2H_6 + H_2O$
7		$2H_2 + CO \rightarrow \frac{1}{2}C_2H_4 + H_2O$
8		$\frac{3}{2}H_2 + CO \rightarrow \frac{1}{2}C_2H_2 + H_2O$
9	H_2O (g)	$H_2 + \frac{1}{2}O_2 \rightarrow H_2O$

The energy of all materials concluded in reactions in Table 19 are calculated by:

$$\Delta H = E_{DFT} + ZPE + \int C_P dT \qquad (15)$$

Where E_{DFT} is the energy from DFT calculations, ZPE is the zero point energy, and $\int C_P dT$ is the integrated heat capacity from 0 to 298 K. Value for these three terms are listed in Table 20.

With enthalpy values in Table 20, we could get the average and standard deviation of reaction enthalpy errors for PBE gas-phase values in reactions containing CO were 0.74609 eV and 0.04595 eV, respectively. For reactions concluding CO_2, the average and standard deviation of reaction enthalpy errors were -0.00890 eV and 0.05008 eV, respectively. In the process of getting corrections for CO and CO_2, we also compared the reaction energies from DFT and experimental reference data for reaction 9 in Table 19 to get the correction for H_2O. All gas-phase energy corrections for the DFT (PBE)

calculations are listed in Table 21.

With the corrected enthalpy values for CO, O_2 and CO_2, we obtained oxygen vacancy formation range as standard for catalytic activity as shown in Figure 4. If the oxide has oxygen vacancy formation energy in the range, it is capable of catalyzing the oxidation reaction of CO spontaneously.

Table 20. Energy from DFT calculations (E_{DFT}), zero-point energy corrections (ZPEs), enthalpic temperature corrections ($\int C_P dT$), and enthalpy (ΔH_{DFT}) for all gas phases [44, 47, 48]

Materials	E_{DFT} (eV)	$\int C_P dT$ (eV)	ZPE (eV)	ΔH_{DFT} (eV)
C_2H_2	-22.9453	0.11	0.72	-22.1153
C_2H_4	-31.9727	0.11	1.36	-30.5027
C_2H_6	-40.5048	0.11	1.98	-38.4148
CH_4	-24.0394	0.1	1.2	-22.7394
H_2	-6.77108	0.09	0.27	-6.41108
H_2O	-13.9011	0.1	0.58	-13.2211
CO_2	-22.9536	0.1	0.31	-22.5436
CO	-14.7762	0.09	0.14	-14.5462
O_2	-9.85917	0.0909	0.1	-9.66827

Table 21. Energy corrections for gas phases and enthalpies before and after correction

Materials	ΔH_{DFT} (eV)	Systematic error (eV)		$\Delta H_{corrected}$ (eV)
CO_2	-22.5436	0.74609		-21.8
CO	-14.5462	-0.0089		-14.56
O_2	-9.66827	non-transition metal	1.0611	-8.61
		transition metal	1.1691	-8.5
H_2O	-13.5389	-0.31781		-13.22

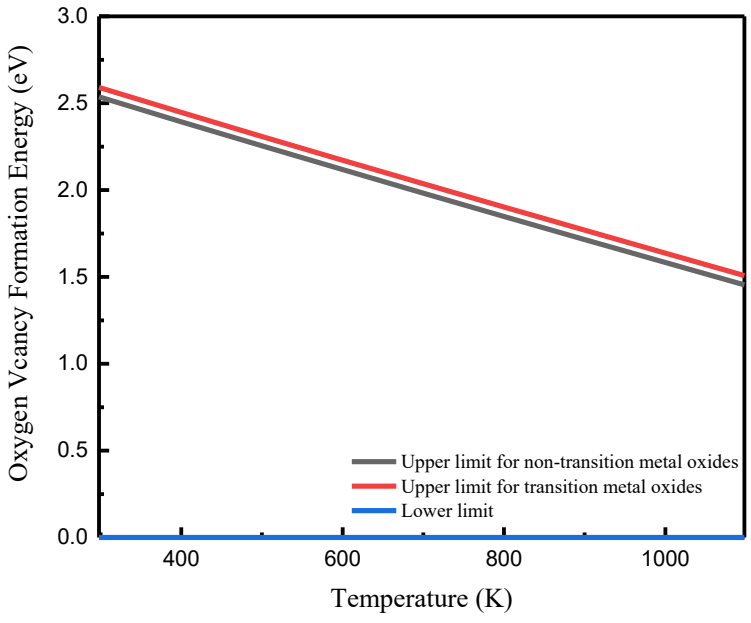

Figure 4. Oxygen vacancy formation energy range

3.3 Stability analysis

Build phase diagram and analyze stability of oxide against gas phases (SO_2, CO, NO, H_2O) by using interfacial reactions, we could plot phase diagram and get interfacial reactions at different temperatures. Comparing the interfacial reaction energies at specific temperature, lowest-reaction-energy reactions for oxides at different temperatures were listed in Table 22.

Table 22. Lowest-energy reactions at different temperatures

Oxides	Temperature	Lowest-energy reactions
As_2O_3	298-598 K	$0.25\ As_2O_3 + NO \rightarrow 0.25As_2O_5 + 0.5N_2O$
	698 K	$0.5\ As_2O_3 + NO \rightarrow 0.5As_2O_5 + 0.5N_2$
Te_4O_9	298-798 K	$0.111\ Te_4O_9 + CO \rightarrow CO_2 + 0.4444Te$
	898-1098 K	$Te_4O_9 + CO \rightarrow CO_2 + 4TeO_2$
$CaRhO_3$	298-798 K	$0.3333\ CaRhO_3 + 0.6667CO \rightarrow 0.3333CaCO_3 + 0.3333CO_2 + 0.3333Rh$
	898-1098 K	$0.5\ CaRhO_3 + 0.5CO \rightarrow 0.5CaCO_3 + 0.25RhO_2 + 0.25Rh$

These lowest-energy reactions could be tested by calculating reaction energy at all temperatures with energies of reactants and products, as shown in Figure 5. For As_2O_3, the lowest-energy reactions kept consistent with Figure 5(a). Reaction energies of reaction 1 is lower than those of reaction 2 from 298 K to 598 K. Reaction 2 has higher energy at 698 K. And both two reactions have positive energy when the temperature is equal to or higher than 798 K. However, for Te_4O_9 and $CaRhO_3$, the calculated reaction energies in Figure 5(b) and 5(c) were not consistent with lowest-energy reactions in Table 22. For Te_4O_9, reaction 1 should have higher energy than reaction 2 at 898 K and

998 K. But Figure 5(b) shows reaction 2 had higher energy at these two temperatures. Similarly, the lowest-energy reaction for $CaRhO_3$ did not match calculated reaction energy at 898 K and 998 K. The inconsistent performance was due to the methods Pymatgen used for reaction energy calculation. To calculate reaction energy, Pymatgen uses energy of the lowest energy equilibrium at desired composition, corresponding to stable phases. For unstable phases, the energy is estimated by using neighboring stable phases. For example, it calculates energy for CO by using energy of CO_2 and C with a ratio of 3:1. N_2O and NO would be unstable at some temperatures. For unstable N_2O, energy is calculated by using energy of N_2 and NO with a ratio of 1:2. For unstable NO, energy is calculated by using energy of N_2O and NO_2 with a ratio of 1:1. But we only consider the partial press of SO_2, H_2O, CO and NO in this study. We should also consider entropy term for other related gases like CO_2 and N_2. The additional gas phase list and partial pressure assignment are shown in Table 23.

Considering all related gas phases by adding their entropy term to free energy, rebuilt phase diagram and did stability analysis. Oxides not reacting with any gas or only reacting with CO are the focuses for next vacancy formation energy calculations. Te_4O_9 and $CaRhO_3$ will react with NO, CO and SO_2 at some temperatures. As_2O_3 will only react with CO. Table 24 shows how As_2O_3 reacts with CO at different temperatures and Figure 6 is the projection of "As-C-S-H-N-O" phase diagram on "As-C-O" phase triangle at 298 K. Besides As_2O_3, there are 31 binary oxides and 36 ABO_3 perovskite structures promising for oxygen vacancy formation energy calculations.

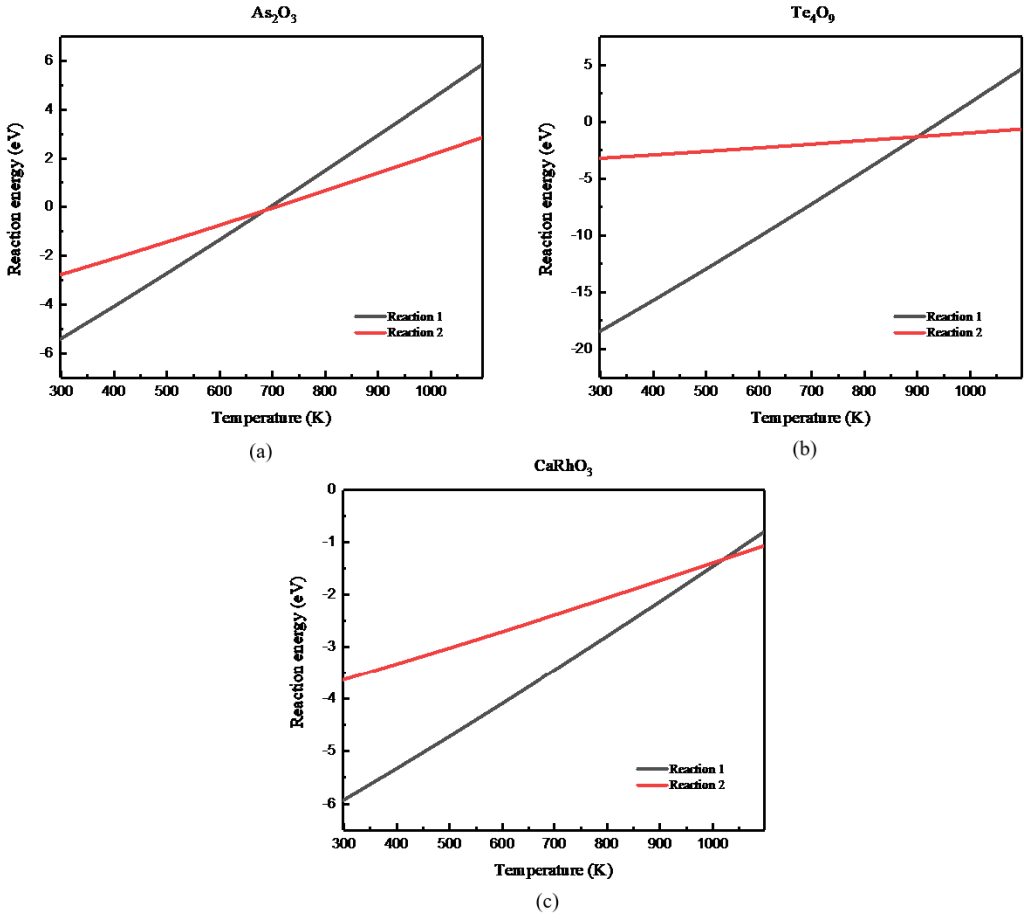

Figure 5. Calculated reaction energy at all temperatures

Table 23. Additional gas phases and partial pressure considered in stability analysis

Gas Phases	Partial Pressure
CO_2	$P_{CO_2} = P_{CO}$
H_2	$P_{H_2} = P_{H_2O}$
H_2O_2	$P_{H_2O_2} = P_{H_2O}$
H_2S	$P_{H_2S} = P_{SO_2}$
H_2SO_4	$P_{H_2SO_4} = P_{SO_2}$
CH_4	$P_{CH_4} = P_{CO}$
N_2	$P_{N_2} = 0.5 \times P_{NO}$
N_2O	$P_{N_2O} = P_{N_2}$
NO_2	$P_{NO_2} = P_{\mathrm{NO}}$
NO_3	$P_{NO_3} = P_{\mathrm{NO}}$
SO_3	$P_{SO_3} = P_{SO_2}$

Table 24. Reactions As_2O_3 reacting against gas phase

Oxide	Against Gas	Temperature (K)	Reaction
As_2O_3	CO	298	$0.25As_2O_3 + 0.75\ CO \rightarrow 0.75\ CO_2 + 0.5As$
	CO	398	$0.25As_2O_3 + 0.75\ CO \rightarrow 0.75\ CO_2 + 0.5As$
	CO	498	$0.25As_2O_3 + 0.75\ CO \rightarrow 0.75\ CO_2 + 0.5As$
	CO	598	$0.25As_2O_3 + 0.75\ CO \rightarrow 0.75\ CO_2 + 0.5As$
	CO	698	$0.25As_2O_3 + 0.75\ CO \rightarrow 0.75\ CO_2 + 0.5As$
	CO	798	$0.25As_2O_3 + 0.75\ CO \rightarrow 0.75\ CO_2 + 0.5As$
	CO	898	$0.25As_2O_3 + 0.75\ CO \rightarrow 0.75\ CO_2 + 0.5As$
	CO	998	$0.25As_2O_3 + 0.75\ CO \rightarrow 0.75\ CO_2 + 0.5As$
	CO	1098	$0.25As_2O_3 + 0.75\ CO \rightarrow 0.75\ CO_2 + 0.5As$

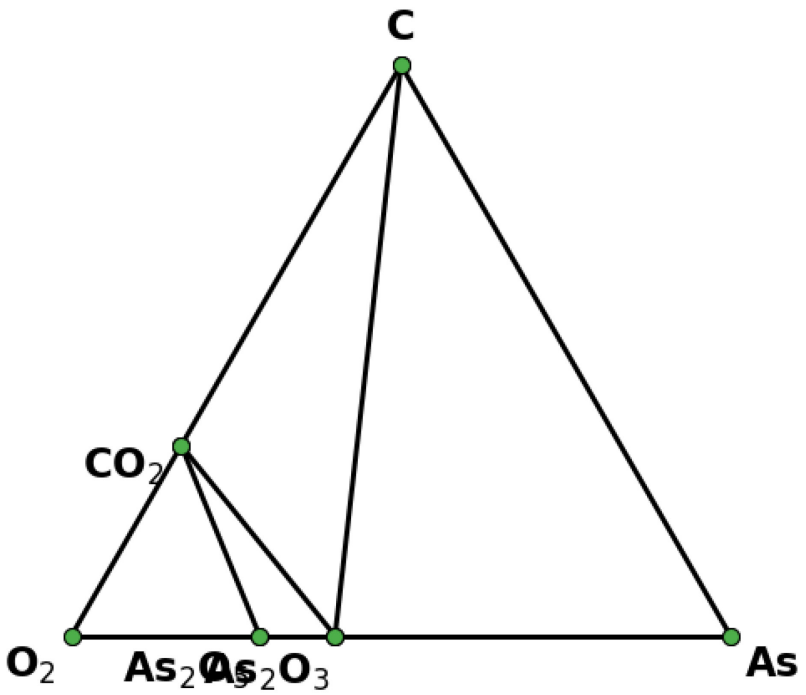

Figure 6. Projection of As-C-S-H-N-O phase diagram on "As-C-O" phase triangle at 298 K

3.4 Oxygen vacancy formation energy

Based on stability analysis, we could calculate the oxygen vacancy formation energy for stable oxides not reacting with SO_2 to find catalyst candidates. Because of confidentiality and effectiveness of the project, not all of the results are shown here. Among the binary oxides and ABO_3 perovskite compounds stable against SO_2, NO and H_2O, some of them have high oxygen vacancy formation energies, like Al_2O_3, BeO, HfO_2, MgO, SiO_2, TiO_2, ZrO_2, $ErAlO_3$, $LiTaO_3$ and so forth, shown in Figure 7. These oxides cannot serve as catalyst for CO treatment. However, there are still promising oxides. For example, Figure 8 shows the oxygen vacancy formation energy on bulk and (1 1 1) surface of one promising candidate. Though bulk oxygen vacancy formation energy is 4.02 eV, around 1.5 eV higher than the upper limit of standard energy range, the oxygen vacancy

formation decreases by 2.07 eV on (1 1 1) surface. As this oxide has appropriate oxygen vacancy formation energy, it is capable of being catalyst for conversion process of CO.

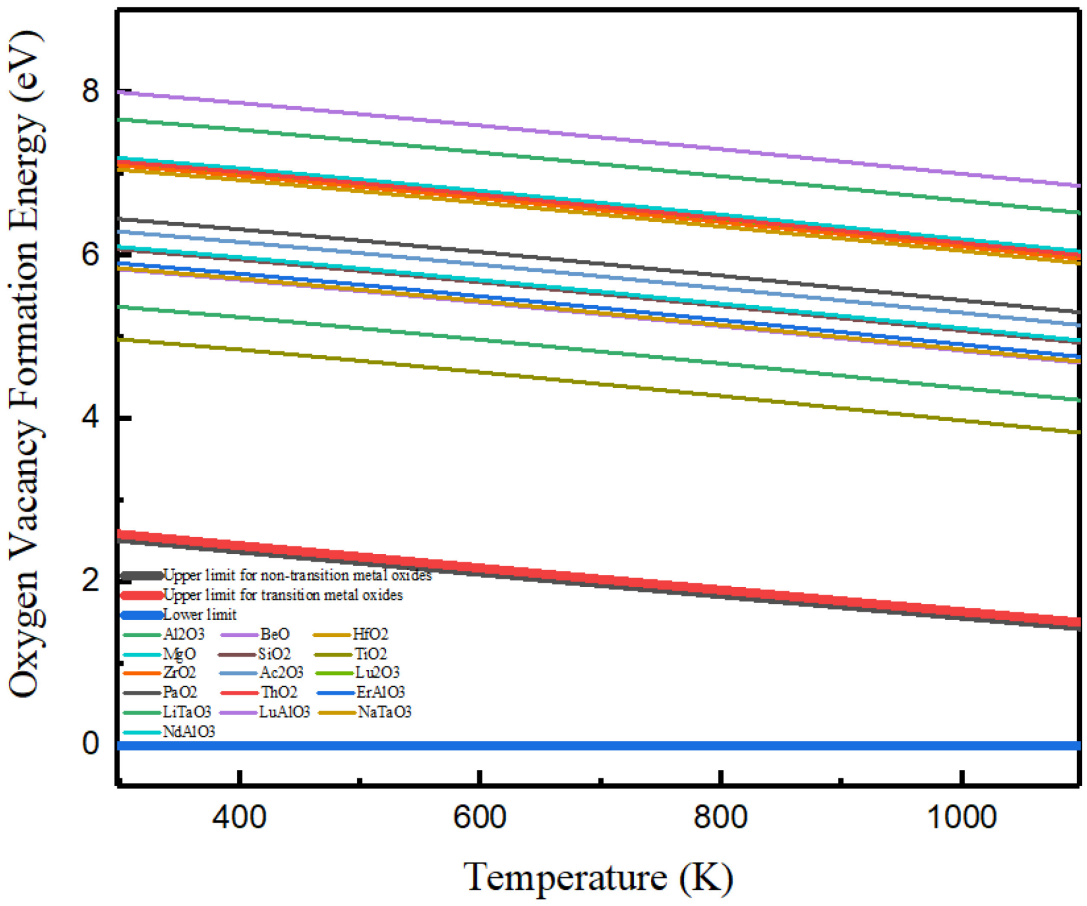

Figure 7. Bulk oxygen vacancy formation energies for some oxides stable against SO_2

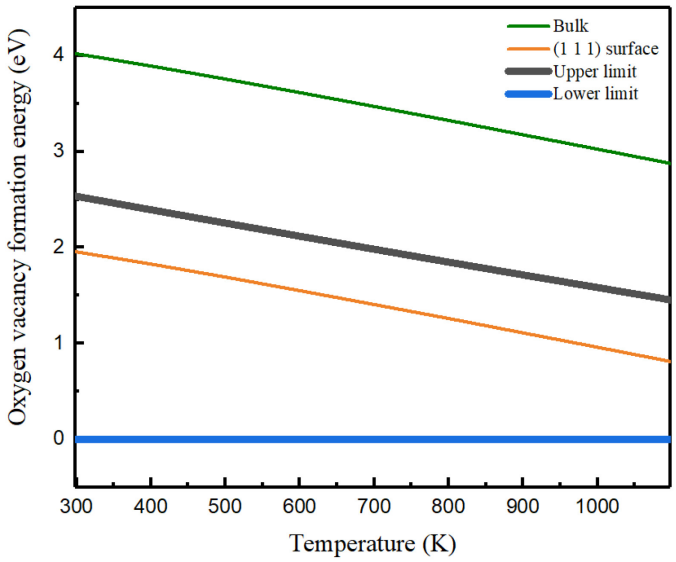

Figure 8. Oxygen vacancy formation energy on bulk and (1 1 1) surface at different temperatures

3.5 Conclusion

In this work, we have conducted stability analysis and DFT + U calculations to study the catalytic activity of oxides for conversion of CO and oxides' resistance to SO_2 at specific environment. Product gas phases should be considered while building phase diagram, which benefits reducing the systematic errors in stability analysis process. In order to test thermodynamic catalytic activity, we got oxygen vacancy formation energy range as criteria and calculated oxygen vacancy formation energy for stable oxides on bulk and surface. Energy corrections for gas phases (CO, CO_2, H_2O and O_2) were used in this process. Though not all catalyst candidates are listed in this paper, promising oxides stable against SO_2 with its appropriate oxygen vacancy formation energy account for the potential as catalytic for exhaust gas treatment. Moreover, taking advantage of interfacial reactions by constructing phase diagram through Pymatgen was proposed as a promising method to test stability of materials in specific gas environment.

References

[1] Air pollution. (n.d.). Retrieved from https://www.who.int/health-topics/air-pollution#tab=tab_1

[2] Ambient (outdoor) air pollution. (n.d.). Retrieved from https://www.who.int/news-room/fact-sheets/detail/ambient-(outdoor)-air-quality-and-health

[3] Household air pollution and health. (n.d.). Retrieved from https://www.who.int/news-room/fact-sheets/detail/household-air-pollution-and-health

[4] Ambient air pollution. (2018, August 28). Retrieved from https://www.who.int/gho/phe/outdoor_air_pollution/en/

[5] World Health Organization. (2006). *Air quality guidelines: global update 2005: particulate matter, ozone, nitrogen dioxide, and sulfur dioxide*. World Health Organization.

[6] Bringing air pollution into the climate change equation. (2014, August 1). Retrieved April 30, 2020, from https://www.who.int/bulletin/volumes/92/8/14-030814/en/

[7] Kampa, M., & Castanas, E. (2008). Human health effects of air pollution. *Environmental pollution*, *151*(2), 362-367.

[8] Levy, R. J. (2015). Carbon monoxide pollution and neurodevelopment: a public health concern. *Neurotoxicology and teratology*, *49*, 31-40.

[9] National Research Council. (2002). *The Ongoing Challenge of Managing Carbon Monoxide Pollution in Fairbanks, Alaska: Interim Report*. National Academies Press.

[10] Review of National Ambient Air Quality Standards for Carbon Monoxide. (2011, August 31). Retrieved April 30, 2020, from http://www.govinfo.gov/content/pkg/FR-2011-08-31/pdf/2011-21359.pdf

[11] History of Reducing Air Pollution from Transportation in the United States. (2020, January 23). Retrieved April 30, 2020, from https://www.epa.gov/transportation-air-pollution-and-climate-

change/accomplishments-and-success-air-pollution-transportation

[12] Timeline of Major Accomplishments in Transportation, Air Pollution, and Climate Change. (2017, January 10). Retrieved April 30, 2020, from https://www.epa.gov/transportation-air-pollution-and-climate-change/timeline-major-accomplishments-transportation-air

[13] United States. (n.d.). Retrieved from https://dieselnet.com/standards/us/index.php

[14] Wikipedia contributors. (2020, April 27). Catalytic converter. In *Wikipedia, The Free Encyclopedia*. Retrieved 15:42, April 30, 2020, from https://en.wikipedia.org/w/index.php?title=Catalytic_converter&oldid=953431671

[15] The three-way catalytic converter. (n.d.). Retrieved April 30, 2020, from https://www.open.edu/openlearn/ocw/mod/oucontent/view.php?printable=1&id=2492

[16] Sharma, S. K., Goyal, P., & Tyagi, R. K. (2016). Conversion efficiency of catalytic converter. *International Journal of Ambient Energy*, *37*(5), 507-512.

[17] Gao, J., Tian, G., Sorniotti, A., Karci, A. E., & Di Palo, R. (2019). Review of thermal management of catalytic converters to decrease engine emissions during cold start and warm up. *Applied Thermal Engineering*, *147*, 177-187.

[18] Wikipedia contributors. (2019, November 30). Catalyst poisoning. In *Wikipedia, The Free Encyclopedia*. Retrieved 15:44, April 30, 2020, from https://en.wikipedia.org/w/index.php?title=Catalyst_poisoning&oldid=928589434

[19] Summers, J. C., & Baron, K. (1979). The effects of SO2 on the performance of noble metal catalysts in automobile exhaust. *Journal of Catalysis*, *57*(3), 380-389.

[20] Emery, A. A., & Wolverton, C. (2017). High-Throughput DFT calculations of formation energy, stability and oxygen vacancy formation energy of ABO 3 perovskites. *Scientific data*, *4*, 170153.

[21] Nolan, M., Fearon, J. E., & Watson, G. W. (2006). Oxygen vacancy formation and migration in ceria. *Solid State Ionics*, *177*(35-36), 3069-3074.

[22] Bergerhoff, G., Hundt, R., Sievers, R., & Brown, I. D. (1983). The inorganic crystal structure data base. *Journal of chemical information and computer sciences*, *23*(2), 66-69.

[23] Belsky, A., Hellenbrandt, M., Karen, V. L., & Luksch, P. (2002). New developments in the Inorganic Crystal Structure Database (ICSD): accessibility in support of materials research and design. *Acta Crystallographica Section B: Structural Science*, *58*(3), 364-369.

[24] A. Jain*, S.P. Ong*, G. Hautier, W. Chen, W.D. Richards, S. Dacek, S. Cholia, D. Gunter, D. Skinner, G. Ceder, K.A. Persson *(*=equal contributions) The Materials Project: A materials genome approach to accelerating materials innovation* APL Materials, 2013, 1(1), 011002.

[25] Kirklin, S., Saal, J. E., Meredig, B., Thompson, A., Doak, J. W., Aykol, M., ... & Wolverton, C. (2015). The Open Quantum Materials Database (OQMD): assessing the accuracy of DFT formation energies. *npj Computational Materials*, *1*(1), 1-15.

[26] Emery, A. A., & Wolverton, C. (2017). High-Throughput DFT calculations of formation energy, stability and oxygen vacancy formation energy of ABO 3 perovskites. *Scientific data*, *4*, 170153.

[27] Kresse, G., & Hafner, J. (1993). Ab initio molecular dynamics for liquid metals. *Physical Review B*, *47*(1), 558.

[28] Perdew, J. P., Burke, K., & Ernzerhof, M. (1996). Generalized gradient approximation made simple. *Physical review letters*, *77*(18), 3865.

[29] Blöchl, P. E. (1994). Projector augmented-wave method. *Physical review B*, *50*(24), 17953.

[30] Wisesa, P., McGill, K. A., & Mueller, T. (2016). Efficient generation of generalized Monkhorst-Pack grids through the use of informatics. *Physical Review*

B, *93*(15), 155109.

[31] Dudarev, S. L., Botton, G. A., Savrasov, S. Y., Humphreys, C. J., & Sutton, A. P. (1998). Electron-energy-loss spectra and the structural stability of nickel oxide: An LSDA+ U study. *Physical Review B*, *57*(3), 1505.

[32] Zhang, L., Bredeson, I., Birenbaum, A. Y., Kent, P. R., Cooper, V. R., Ganesh, P., & Xu, H. (2018). Oxygen vacancy formation energies in PbTiO 3/SrTiO 3 superlattice. *Physical Review Materials*, *2*(6), 064409.

[33] Hinuma, Y., Toyao, T., Kamachi, T., Maeno, Z., Takakusagi, S., Furukawa, S., ... & Shimizu, K. I. (2018). Density functional theory calculations of oxygen vacancy formation and subsequent molecular adsorption on oxide surfaces. *The Journal of Physical Chemistry C*, *122*(51), 29435-29444.

[34] Tanaka, I., Oba, F., Tatsumi, K., Kunisu, M., Nakano, M., & Adachi, H. (2002). Theoretical formation energy of oxygen-vacancies in oxides. *Materials Transactions*, *43*(7), 1426-1429.

[35] Ong, S. P., Wang, L., Kang, B., & Ceder, G. (2008). Li− Fe− P− O2 phase diagram from first principles calculations. *Chemistry of Materials*, *20*(5), 1798-1807.

[36] Wikipedia contributors. (2020, April 14). Phase diagram. In *Wikipedia, The Free Encyclopedia*. Retrieved 15:49, April 30, 2020, from https://en.wikipedia.org/w/index.php?title=Phase_diagram&oldid=950958371

[37] (n.d.). Retrieved April 30, 2020, from http://www.eng.usf.edu/~campbell/ThermoI/Proptut/tut1.html

[38] Q. (2017, September 30). Convex hull and compositional phase diagram. Retrieved from https://github.com/qzhu2017/CMS/wiki/Convex-hull-and-compositional-phase-diagram

[39] Porter, D. A., Easterling, K. E., & Sherif, M. (2009). *Phase transformations in metals and alloys (revised reprint)*. CRC press.

[40] (n.d.). Retrieved April 30, 2020, from

https://materialsproject.org/docs/interfacerxns

[41] pymatgen.analysis.interface_reactions module. (n.d.). Retrieved April 30, 2020, from https://pymatgen.org/pymatgen.analysis.interface_reactions.html?highlight=interfacialreactivity#pymatgen.analysis.interface_reactions.InterfacialReactivity

[42] Introduction. (n.d.). Retrieved April 30, 2020, from https://pymatgen.org/introduction.html

[43] NIST Office of Data and Informatics. (n.d.). NIST Chemistry WebBook, SRD 69. Retrieved April 30, 2020, from https://webbook.nist.gov/chemistry/

[44] Cao, L., Raciti, D., Li, C., Livi, K. J., Rottmann, P. F., Hemker, K. J., ... & Wang, C. (2017). Mechanistic insights for low-overpotential electroreduction of CO2 to CO on copper nanowires. *ACS Catalysis*, *7*(12), 8578-8587.

[45] Wang, L., Maxisch, T., & Ceder, G. (2006). Oxidation energies of transition metal oxides within the GGA+ U framework. *Physical Review B*, *73*(19), 195107.

[46] Li, C., Raciti, D., Pu, T., Cao, L., He, C., Wang, C., & Mueller, T. (2018). Improved Prediction of Nanoalloy Structures by the Explicit Inclusion of Adsorbates in Cluster Expansions. *The Journal of Physical Chemistry C*, *122*(31), 18040-18047.

[47] Medvedev, V. A., Cox, J. D., & Wagman, D. D. (Eds.). (1989). *CODATA key values for thermodynamics*. New York: Hemisphere Publishing Corporation.

[48] Rahal, M., Hilali, M., El Hammadi, A., El Mouhtadi, M., & El Hajbi, A. (2001). Calculation of vibrational zero-point energy. *Journal of Molecular Structure: THEOCHEM*, *572*(1-3), 73-80.